Nanoscale to microscale reversal in room-temperature plasticity in $SrTiO_3$ by tuning defect concentration

Xufei Fang[1]*, Kuan Ding[1], Stephan Janocha[1], Christian Minnert[1], Wolfgang Rheinheimer[1], Karsten Durst[1]*, Atsutomo Nakamura[2,3]*, Jürgen Rödel[1]

[1]Department of Materials and Earth Sciences, Technical University of Darmstadt, 64287 Darmstadt, Germany

[2]Department of Materials Physics, Nagoya University, Furo-cho, Chikusa-ku, Nagoya 464-8603, Japan

[3]PRESTO, Japan Science and Technology Agency (JST), 7, Gobancho, Chiyoda-ku, Tokyo 102-0076, Japan

---

*Corresponding authors: fang@ceramics.tu-darmstadt.de (X.F.); k.durst@phm.tu-darmstadt.de (K.D.); anaka@nagoya-u.jp (A.N.).

Abstract

Incipient room-temperature plastic deformation in $SrTiO_3$ at the nanoscale and the microscale is contrasted by applying a scale-dependent indentation technique. Using nanoindentation pop-in, nanoindentation creep, and an evaluation of dislocation spacing via etch pit study, we demonstrate a reversal of yield stress for crystals with different vacancy concentrations and pre-existing dislocation densities. A competing mechanism between dislocation nucleation and dislocation motion on crystal plasticity at different length scales is highlighted. This finding enables us to complete the understanding of dislocation-mediated plasticity for ceramic oxides at the nanoscale as compared to the microscale and macroscale.

Keywords: defects, room-temperature plasticity, dislocation nucleation and motion, nanoindentation, $SrTiO_3$

Graphical Abstract:

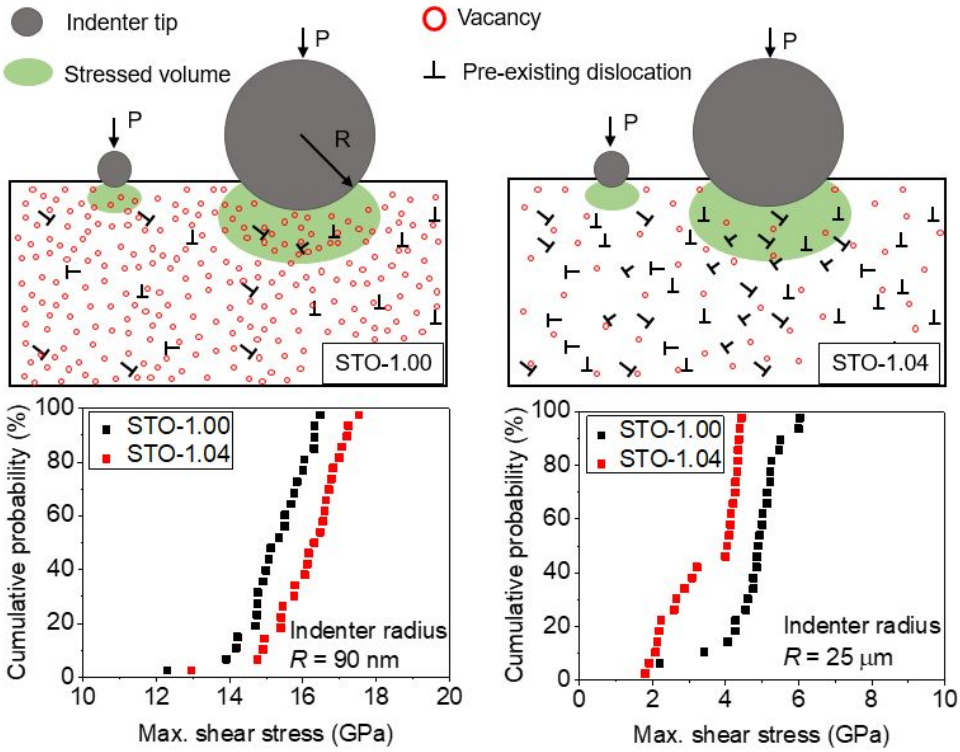

I. Introduction

Crystal defects such as vacancies (0-dimensional) and dislocations (1-dimensional) play critical roles in determining functional properties in ceramics. For instance, dislocations in ceramics have demonstrated enormous potential to tune electrical conductivity [1], thermal conductivity [2, 3], and ferroelectric hardening [4]. While in the last decades nanoscale defects were used to tune functional properties of bulk oxides [5, 6], corresponding nanoscale concepts had been mostly neglected in the area of mechanical properties of ceramics. The vast majority of ceramics are known to be of brittle nature at room temperature. The strong ionic and covalent bonding states, as well as the very low numbers of dislocations (sources), yield limited or no plasticity, which greatly impairs the mechanical reliability in application.

The few ceramics that can be plastically deformed as single crystal at room temperature have been tagged as “surprising” for $SrTiO_3$ [7], “unexpected” for $KNbO_3$ [8], and “extraordinary” for ZnS [9]. Yet little effort has been made to actively tune the plasticity in ceramics compared to metallic materials [10, 11]. In a recent ground-breaking work, room temperature plasticity of ceramics was tuned by changing the cation ratio in $SrTiO_3$ [12]. In comparison to samples with Sr/Ti=1.00, the samples with Sr/Ti=1.04 in the starting powders exhibit lower yield strength (~15% decrease) and much higher fracture strain (~70% increase). However, a fundamental understanding of the basic dislocation mechanisms (dislocation nucleation, multiplication, and motion) as well as scale-dependent plasticity remained elusive.

In contrast to bulk testing, nanoindentation has been proven a powerful tool owing to the small volume requirement, high throughput, and fast screening capabilities. Besides the determination of mechanical properties such as Young’s modulus and hardness, it can be used to unmask the fundamental dislocation mechanisms involved in the local plasticity [13-15], with a majority of studies focusing on metallic materials. For ceramics, due to the brittle nature and frequent occurrence of fracture, indentation as a means to interrogate local plasticity has been less investigated. Some representative nanoindentation studies in ceramics can be found in MgO [16-18], CaF_2 [19, 20], ZnO [21], and $SrTiO_3$ [22-24], yet no attempt has been made to address the scale-dependent plasticity with respect to varying defect concentrations.

$SrTiO_3$, as a model perovskite oxide, has been known as a "soft" oxide that can be plastically deformed at room temperature. In addition to bulk deformation [25-27], Javaid et al. [22-24] have systematically investigated the indentation size effect and 3D dislocation structure of $SrTiO_3$. The slip system of single-crystal $SrTiO_3$ at room temperature has been reported to be <110>{110} [25-27].

In order to pave the road for active engineering of room temperature plasticity of ceramics, the fundamentals of dislocation mechanics in oxides need to be understood first. We focus on $SrTiO_3$ as a model system in this study to advance the understanding applicable to ceramics in general. Samples with Sr/Ti=1.00 and Sr/Ti=1.04 (details see *Material & Method* at the end) with different vacancy concentrations and dislocation densities are used to understand the defect-based plasticity.

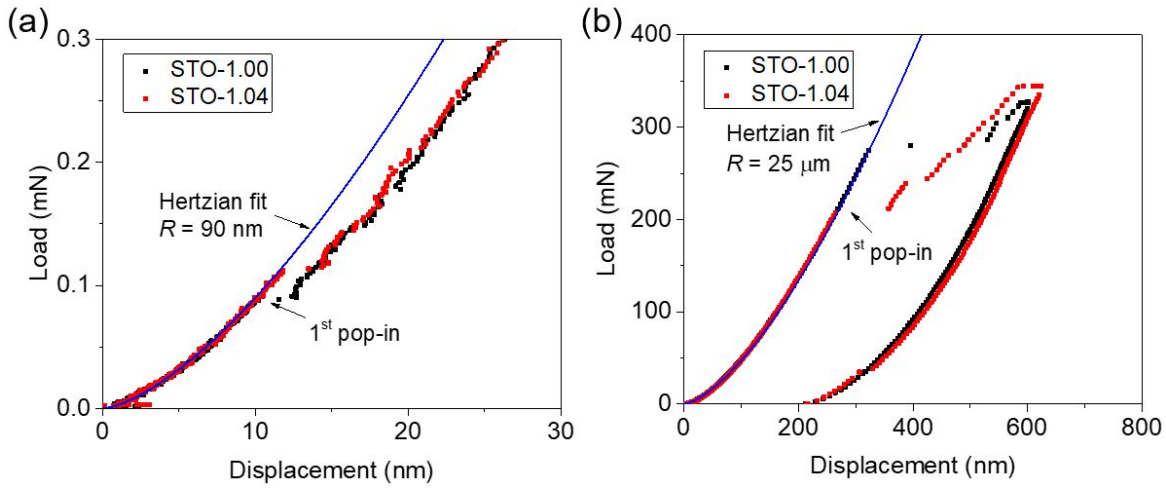

Fig.1 Representative load-displacement curves highlight scale-dependent deformation with pop-in event corresponding to the incipient plasticity: (a) small indenter radius *R* = 90 nm; (b) large indenter radius *R* = 25 μm. The elastic portions for STO-1.00 and STO-1.04 are well overlapped, indicating an identical elastic modulus.

We address scale-dependent plasticity from the nanometer range to microscale range (see scale analysis in Table S1 in Supporting Information) in order to unveil scale interactions between ensuing stress field and local microstructure. We start by presenting representative indentation pop-in (the sudden displacement burst) in the load-displacement curves featuring nanoscale plasticity for a small indenter

(R = 90 nm) (Fig.1a) and a large indenter (R = 25 μm) for microscale plasticity (Fig.1b). Prior to the pop-in, the stressed volume undergoes purely elastic deformation, which can be described by the Hertzian fit [28]:

$$P = \frac{4}{3} E_r \sqrt{R} h^{3/2} \quad (1)$$

The reduced modulus E_r is calculated from the elastic constants of the indenter and the specimen by $\frac{1}{E_r} = \frac{1-v_i^2}{E_i} + \frac{1-v_s^2}{E_s}$, with E_i =1140 GPa and v_i =0.07 for the diamond tip, E_s =264 GPa [27] and v_s =0.237 [24] for $SrTiO_3$. The indenter radius is fitted with the Hertzian analysis.

It has been widely accepted in metallic materials that the initial pop-in (in a dislocation-starved region) corresponds to the dislocation nucleation. In brittle oxides, however, care must be taken since cracking or phase transformation could also result in a strain burst or pop-in [29]. Here the room temperature deformation involves no phase transformation in $SrTiO_3$. Furthermore, in single-crystal $SrTiO_3$, dislocation-mediated plasticity occurs prior to crack initiation, as verified by previous experiments with compelling proof from *in situ* TEM study by Kondo et al.[30] and etch pit study by Javaid et al.[23]. Hence the onset load of the first pop-in (Fig.1) allows the computation of the maximum shear stress, $\tau_{\max}$, which is responsible for dislocation activation beneath the indenter during deformation, by following Ref. [28]:

$$\tau_{\max} = 0.31 \left(\frac{6E_r^2}{\pi^3 R^2} P_{pop-in}\right)^{1/3} \quad (2)$$

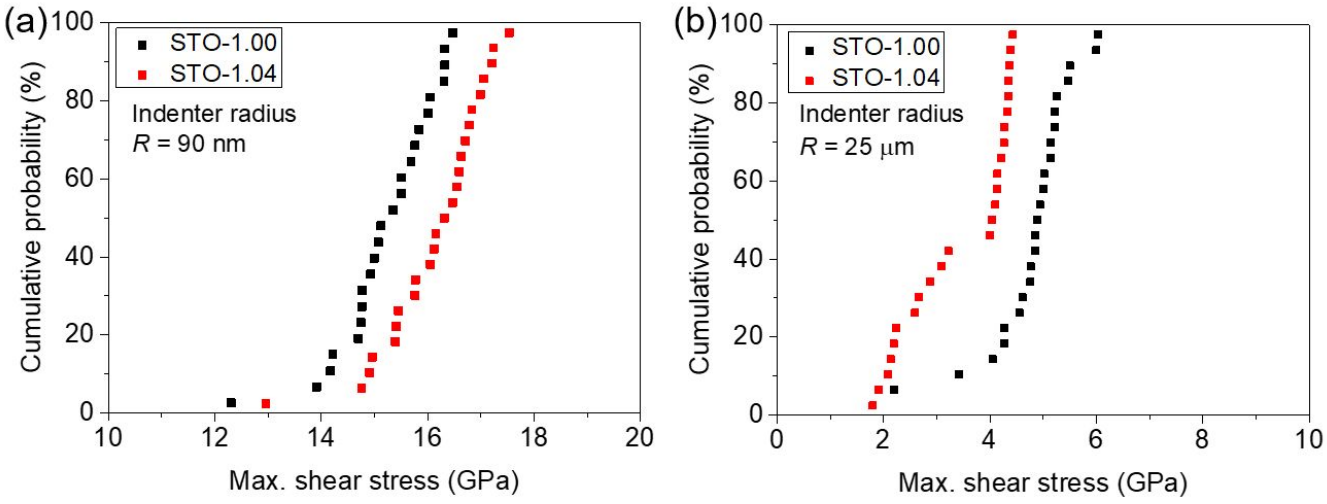

Fig.2 Comparison of the statistical distribution (25 indents each) of maximum shear stress using (a) indenter radius R = 90 nm; and (b) indenter radius R = 25 μm.

Figure 2 ascertains the "indentation pop-in size effect" [13, 14], namely, for both samples, the maximum shear stress is much larger for small indenter (R = 90 nm) than that for large indenter (R = 25 μm). Strikingly, the change of scale further reverses the order of maximum shear stress under two different indenter radii. The STO-1.04 with macroscopically lower yield stress [12] features a lower shear stress on the microscale (R = 25 μm) but a higher shear stress on the nanoscale (R = 90 nm).

Let us first consider the impact of pre-existing dislocation density. Etch pit study reveals that the pre-existing dislocation density in the pristine STO-1.00 is ~10^{10} m^{-2} and ~10^{11} m^{-2} for STO-1.04 (Fig. S1 in Supporting Information). For indentation with small radius R = 90 nm, pop-in is most likely to occur in a dislocation-free region (Fig. S2) considering the pre-existing dislocation density. Hence, homogeneous dislocation nucleation is considered the dominating process in the pop-in event [19], resulting in a maximum shear stress (14-17.5GPa in Fig. 2a, which is G/8-G/6, with G being the shear modulus of $SrTiO_3$) close to the estimated theoretical strength (~G/2π) [31, 32]. Note that even with the small indenter, there is a chance that pre-existing dislocations or surface asperities existed in the stressed volume. These events are likely to result in a lower maximum shear stress, as evidenced by the tail of the probability distribution of the maximum shear stresses in Fig. 2a.

For R = 25 μm, there is a much higher chance of probing pre-existing dislocations in the stressed volume (Fig. S2), resulting in heterogeneous dislocation nucleation and/or motion of pre-existing dislocations, yielding a much lower maximum shear stress (2-6GPa in Fig. 2b). In ceramics, such effect of pre-existing dislocations on the plastic deformation was previously reported on CaF_2 by Lodes et al.[20] using nanoindentation experiments and molecular dynamic simulations.

However, the impact of pre-existing dislocations does not suffice to rationalize the intriguing reverse trend of the maximum shear stress for STO-1.00 and STO-1.04 under different tip radii (Fig.1). In addition to the lower dislocation density, STO-1.00 is expected to have a higher Sr and O vacancy concentration due to the different chemical composition (*Material & Method*). As vacancies are known to ease dislocation nucleation [33, 34], the higher vacancy concentration of STO-1.00 is suggested responsible for the lower maximum shear stress for dislocation nucleation in comparison to STO-1.04 for the nanoscale plasticity beneath the indenter with R = 90 nm.

The above explanation considering both pre-existing dislocations and vacancies is schematically illustrated in Fig. 3. According to Bei et al.[15], for large indenters such as R = 25 μm, the microscopic plasticity resembles the macroscopic plasticity. Therefore, based on the pop-in stress obtained from R = 25 μm, one can expect a lower yield stress for bulk STO-1.04. This prediction is confirmed by the excellent agreement with the bulk compression test probing sample size of 3 mm x 3 mm x 7.5 mm [12].

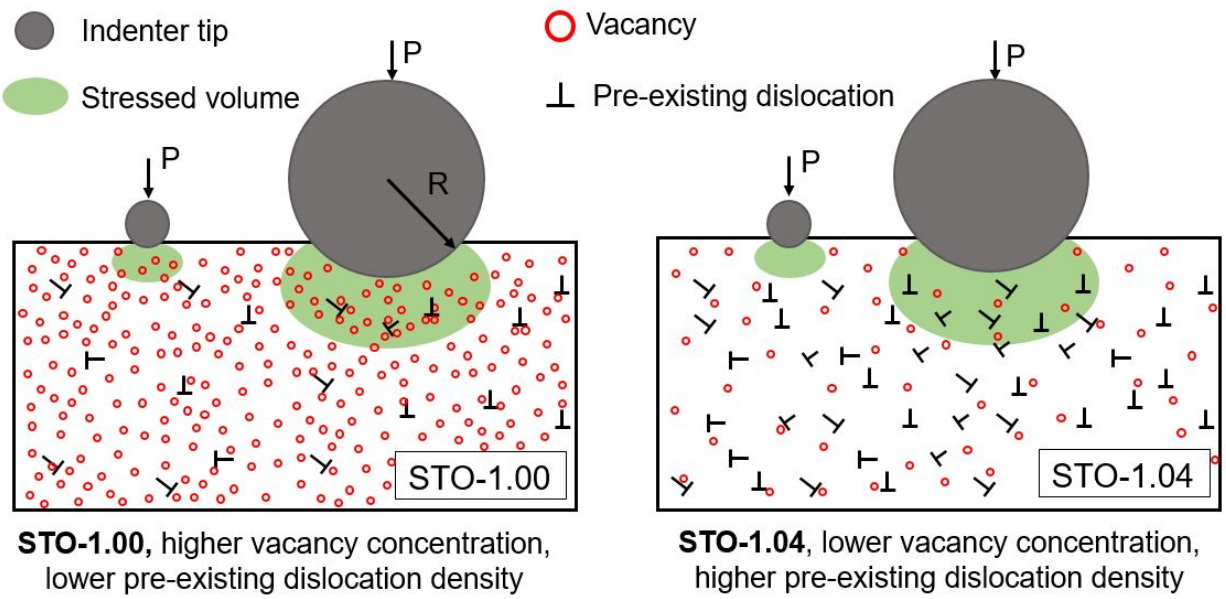

Fig.3 Schematic of the mechanism map featuring the competing effect between the pre-existing vacancy concentration and dislocation density for the homogeneous dislocation nucleation (small indenter, nanoscale) and the heterogeneous dislocation nucleation or activation of pre-existing dislocations (large indenter, microscale).

Additionally, during pop-in for the large indenters, the motion of pre-existing dislocations becomes pertinent. To this end, the movement of pre-existing dislocations in STO-1.00 and STO-1.04 was quantified using creep tests. The indentation creep strain is defined as $\varepsilon = \frac{\Delta h}{h} = \frac{h - h_0}{h}$, with h being the current depth and h_0 being the starting depth of the constant load hold stage [35, 36]. The creep strain rate is obtained by differentiating ε with time. Note that the nanoindentation hardness at the beginning of the constant load hold is ~15 GPa for both STO-1.04 and STO-1.00. This value is identical to that reported for (001) $SrTiO_3$ by Javaid et al. [23] at the same indentation depth (~100 nm).

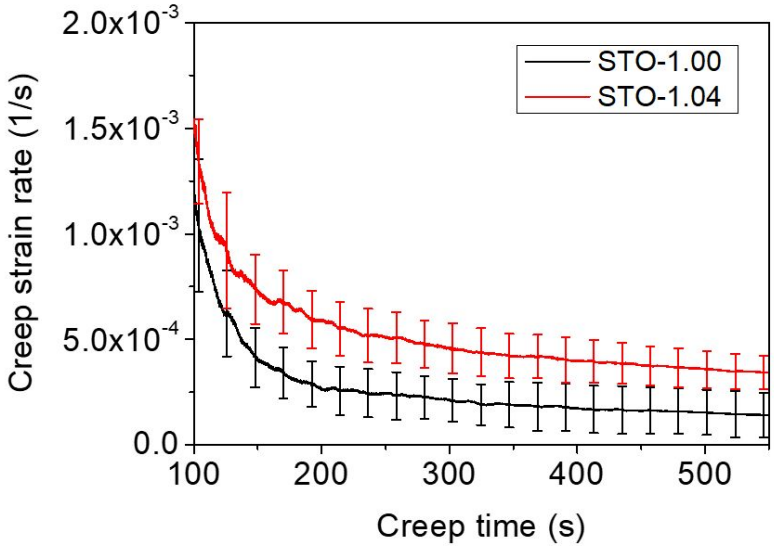

Fig. 4 Nanoindentation creep strain rate as function of time. Each curve is averaged on 10 tests, with error bars presented for a time interval of 25 s.

The averaged (over 10 tests for each condition) indentation creep strain rates as function of time are displayed in Fig. 4, featuring a higher creep strain rate of STO-1.04, which is almost two times that of STO-1.00. The origin of the higher creep strain rate in STO-1.04 is suggested to lie in the different defect chemistry. As discussed above, STO-1.00 has a higher Sr and O vacancy concentration due to Sr evaporation during processing. In STO-1.04, the Sr excess in the starting powder was adjusted to compensate for this loss. In $SrTiO_3$, segregation of Sr vacancies is well known for interfaces such as grain boundaries [37, 38]. For similar thermodynamic reasons, vacancies could also segregate to dislocations as reported [39, 40]. As cations are immobile in $SrTiO_3$ at room temperature [41, 42], Sr vacancies are not following the dislocation migration and, hence, cannot result in solute drag. However, oxygen diffusion is very fast even at room temperature [43]. Accordingly, oxygen vacancies are suggested to segregate at dislocations, leading to solute drag of the dislocations and a higher friction stress in STO-1.00, where more oxygen vacancies are present. An analogous mechanism was reported recently for dislocation motion in ZrO_2, where fast oxygen vacancies segregate to dislocations [44], and for hydrogen embrittlement, where hydrogen aggregation at dislocations is believed to result in the hardening effect [45].

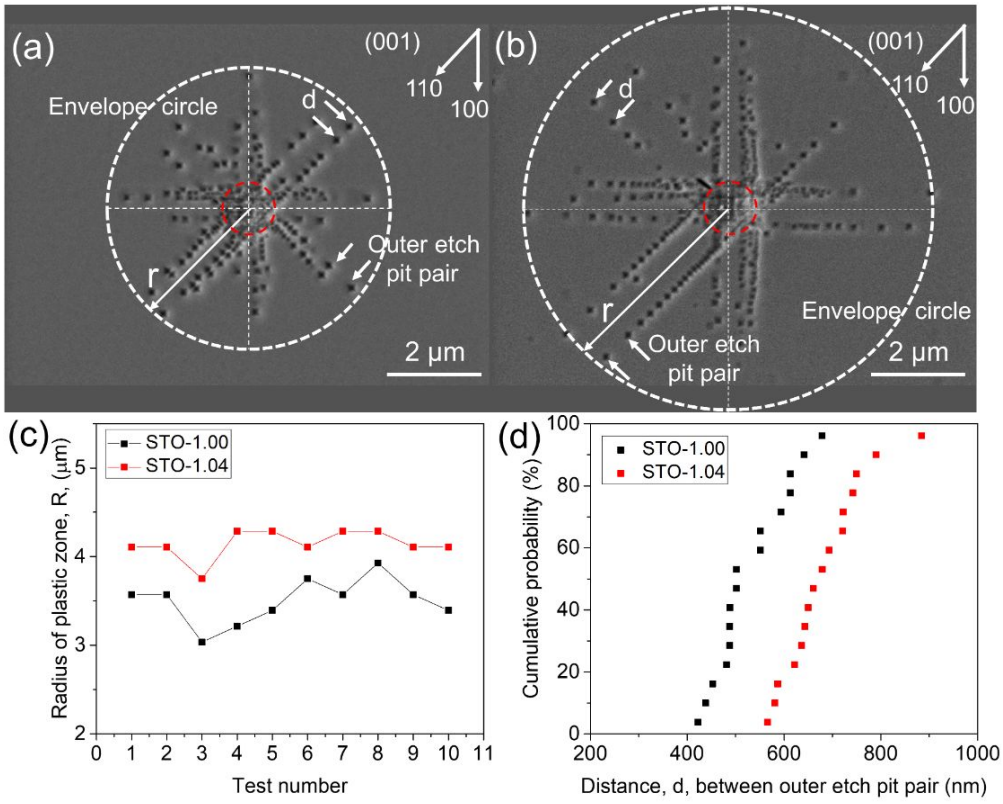

Fig. 5 (a) Etch pits on STO-1.00; (b) STO-1.04 for R = 2 μm. The red dashed circles indicate the contact circle of the indenter tip on the sample surface. The white dashed circles indicate the envelope of the plastic zone. (c) Comparison of the plastic zone size for STO-1.00 and STO-1.04. (d) Comparison of the distance for the outer dislocation pairs in the <110> dislocation pile-ups. Note a grey background in (a-b) is used to highlight the white enveloping circle as it goes beyond the original SEM image.

In order to further confirm the lower lattice friction stress in STO-1.04, we conducted a study on etch pits of indents using a tip with R = 2 μm, which inhibits the cracking in both STO-1.00 and STO-1.04 (Fig.5a, b) under the same maximum displacement of 140 nm with a corresponding load of ~11 mN.

The method for quantification of lattice friction stress was first proposed by Gaillard et al. on MgO [16] using the dislocation etch pits in isolated pile-ups. Following this model, the dislocation spacing in the indentation residual impression quantifies the stress balance. Shortly put, under equilibrium condition, the shear stress acting on the dislocation in a pile-up arm is given by $\tau_a - \tau_f + \tau_d + \tau_{im} = 0$, where τ_a is

the applied shear stress from the indentation, τ_f is the lattice friction stress, τ_d is the dislocation-dislocation interaction stress, and τ_{im} the surface image stress [16]. For the current analysis, we consider the dislocation etch pit pile-ups in the <110> direction (Fig. 5a, b). In this specific pile-up direction, the emerging dislocations have pure edge character lying on {110} glide planes perpendicular to the (001) surface [22]. In this case, the image force τ_{im} is 0. A direct application from Gaillard's model is that, given the same loading conditions on both samples, a lower lattice friction stress gives a larger plastic zone, indicated by the dislocation travelling distance in the radial direction (half radius of the white dashed envelope circle that encapsulates all the dislocation etch pits in Fig. 5c, d) and a larger spacing between the outermost dislocation pair in single pile-up arms (short white arrow pairs in Fig. 5a, b). This offers a straightforward approach to qualitatively evaluate the lattice friction stress based on the etch pit study. The distribution of the radius, r, for 10 indents on both samples is given in Fig. 5c (details given in Fig.S3 and Fig.S4). A clear trend is seen that STO-1.04 has a larger travelling distance for the dislocations being activated. Correspondingly, the distance, d, between the outermost etch pit pair is larger in STO-1.04, based on the measurement of 16 pile-up arms. The creep tests and etch pit study consistently provide compelling proof for higher lattice barrier for the dislocation motion in STO-1.00.

In summary, we provide compelling demonstration for reversing the order of yield stress in going from nanoscale to microscale by altering defect concentrations in $SrTiO_3$. $SrTiO_3$ with higher Sr and O vacancy concentration favors dislocation nucleation and yields a lower maximum shear stress in nanoscale indentation; while the lower pre-existing dislocation density results in a higher maximum shear stress in microscale plasticity. This reversal is rationalized by the higher friction stress caused by the solute drag by higher concentration of O vacancies. The competition between the dislocation nucleation dominated nanoscale plasticity and the dislocation motion dominated microscale plasticity is explained. Our findings have important implications for active tuning of mechanical properties for ceramic oxides at both nanoscale, microscale, and macroscale via defect engineering [12].

Materials & Methods

$SrTiO_3$ single crystals, grown by the Verneuil method from high purity $SrTiO_3$ powder (99.9 wt %) and high purity $SrCO_3$ powder (99.99 wt %), were used (Shinkosha Co., Ltd., Yokohama, Japan). Single crystals grown using starting powders with Sr/Ti = 1.00 and Sr/Ti = 1.04 were selected. Typically, Sr deficiency is induced during crystal growth of $SrTiO_3$ crystals due to the evaporation of Sr ahead of the solidification front resulting in the formation of Sr vacancies in the single crystals because of their low formation energy [46, 47]. Therefore, a single crystal with the starting composition of Sr/Ti = 1.04 was used to achieve a lower concentration of Sr vacancies [12]. The two crystals are labelled as STO-1.00 and STO-1.04, respectively. Due to charge compensation, for negative point defects as Sr vacancies, the formation of oxygen vacancies is favored particularly during high temperature processing [48]. Accordingly, the STO-1.00 is assumed to have a high concentration of Sr and O vacancies, while STO-1.04 has lower concentrations of these point defects. However, we note that the quantification of the true concentration of these vacancies remains extremely challenging [5].

All indentation tests were performed on (001) surface of bulk samples with a size of about 3 mm x 3 mm x 7 mm. The average surface roughness measured by Atomic Force Microscopy (AFM) is less than 1 nm. The specimens were etched for 20 s in 10 mL 65% HNO_3 with a few drops of 40% HF to reveal dislocations [24]. Indention pop-in study was carried out using the continuous stiffness measurement (CSM) mode with a constant strain rate of 0.05 s^{-1} on a G200 nanoindenter (Keysight Technologies, USA), which allows for using various tip radii from a diamond Berkovich indenter (with an effective indenter radius R = 90 nm) to spherical indenters with R = 2 µm and R = 25 µm (Synton MDP, Switzerland). A harmonic displacement oscillation of 2 nm was applied with a frequency of 45 Hz. Creep tests with a diamond Berkovich tip were performed with the iNano system (Nanomechanics inc., USA) due to the better force and displacement resolution. The CSM based constant load and hold method (CLH, developed by Maier et al. [49]) was used. In the initial loading segment, an indentation strain rate 0.02 s^{-1} was applied until the load 3 mN (depth ~100 nm) was reached. Afterwards, the load was kept constant for 600 s. In this case,

the harmonic displacement of 2 nm was applied with a frequency of 100 Hz. For each condition of creep tests, at least 10 tests were performed and later averaged for comparison. For all tests with Berkovich tips, frame stiffness and tip area functions were calibrated on a fused silica reference according to Oliver-Pharr method [50]. The etch pits were characterized using a TESCAN MIRA3 Scanning Electron Microscope (SEM, Brno, Czech Republic).

Acknowledgement

We thank Dr. Enrico Bruder for the assistance on SEM, and Lukas Porz for discussion. X. Fang gratefully acknowledges the Athene Young Investigator Program at TU Darmstadt. K. Durst (DFG, DU 424/11-1) and J. Rödel (DFG, No. 414179371) thank the Deutsche Forschungsgemeinschaft for financial support. A. Nakamura acknowledges the financial support of JST PRESTO Grant Number JPMJPR199 and JSPS KAKENHI Grant Numbers JP19H05786, JP17H06094 and JP18H03840, Japan.

Supporting information

Please find supporting figures and table in separated file.

Conflict of interests

The authors declare no conflict of interests.

Data availability

The data is available upon reasonable request from the corresponding author (X.F.).

References

1. Nakamura, A.; Matsunaga, K.; Tohma, J.; Yamamoto, T.; Ikuhara, Y. *Nature Materials* **2003,** 2, (7), 453-6.

2. Khafizov, M.; Pakarinen, J.; He, L.; Hurley, D. H. *Journal of the American Ceramic Society* **2019**.

3. Sun, B.; Haunschild, G.; Polanco, C.; Ju, J. Z.; Lindsay, L.; Koblmuller, G.; Koh, Y. K. *Nature Materials* **2019,** 18, (2), 136-140.

4. Ren, P.; Höfling, M.; Koruza, J.; Lauterbach, S.; Jiang, X.; Frömling, T.; Khatua, D. K.; Dietz, C.; Porz, L.; Ranjan, R.; Kleebe, H. J.; Rödel, J. *Journal of the American Ceramic Society* **2019**.

5. Gunkel, F.; Christensen, D. V.; Chen, Y. Z.; Pryds, N. *Applied Physics Letters* **2020,** 116, 120505.

6. Ikuhara, Y. *Progress in Materials Science* **2009,** 54, (6), 770-791.

7. Brunner, D.; Taeri-Baghbadrani, S.; Sigle, W.; Rühle, M. *Journal of the American Ceramic Society* **2001,** 84, (5), 1161-1163.

8. Mark, A. F.; Castillo-Rodriguez, M.; Sigle, W. *Journal of the European Ceramic Society* **2016,** 36, (11), 2781-2793.

9. Oshima, Y.; Nakamura, A.; Matsunaga, K. *Science* **2018,** 360, 772-774.

10. Greer, J. R.; De Hosson, J. T. M. *Progress in Materials Science* **2011,** 56, (6), 654-724.

11. Li, X.; Lu, K. *Nature materials* **2017,** 16, (7), 700-701.

12. Nakamura, A.; Yasufuku, K.; Furushima, Y.; Toyoura, K.; Lagerlöf, K.; Matsunaga, K. *Crystals* **2017,** 7, (11), 351.

13. Shim, S.; Bei, H.; George, E. P.; Pharr, G. M. *Scripta Materialia* **2008,** 59, (10), 1095-1098.

14. Morris, J. R.; Bei, H.; Pharr, G. M.; George, E. P. *Physical Review Letters* **2011,** 106, (16).

15. Bei, H.; Xia, Y. Z.; Barabash, R. I.; Gao, Y. F. *Scripta Materialia* **2016,** 110, 48-52.

16. Gaillard, Y.; Tromas, C.; Woirgard, J. *Acta Materialia* **2006,** 54, (5), 1409-1417.

17. Montagne, A.; Audurier, V.; Tromas, C. *Acta Materialia* **2013,** 61, (13), 4778-4786.

18. Amodeo, J.; Merkel, S.; Tromas, C.; Carrez, P.; Korte-Kerzel, S.; Cordier, P.; Chevalier, J. *Crystals* **2018,** 8, (6), 240-292.

19. Lorenz, D.; Zeckzer, A.; Hilpert, U.; Grau, P.; Johansen, H.; Leipner, H. S. *Physical Review B* **2003,** 67, (17).

20. Lodes, M. A.; Hartmaier, A.; Göken, M.; Durst, K. *Acta Materialia* **2011,** 59, (11), 4264-4273.

21. Bradby, J. E.; Kucheyev, S. O.; Williams, J. S.; Jagadish, C.; Swain, M. V.; Munroe, P.; Phillips, M. R. *Applied Physics Letters* **2002,** 80, (4537).

22. Javaid, F.; Stukowski, A.; Durst, K. *Journal of the American Ceramic Society* **2017,** 100, (3), 1134-1145.

23. Javaid, F.; Bruder, E.; Durst, K. *Acta Materialia* **2017,** 139, 1-10.

24. Javaid, F.; Johanns, K. E.; Patterson, E. A.; Durst, K. *Journal of the American Ceramic Society* **2018,** 101, (1), 356-364.

25. Gumbsch, P.; Taeri-Baghbadrani, S.; Brunner, D.; Sigle, W.; Ruhle, M. *Physical Review Letters* **2001,** 87, (8), 085505.

26. Taeri, S.; Brunner, D.; Sigle, W.; Rühle, M. *Z. Mettllkd.* **2004,** 95, (6).

27. Patterson, E. A.; Major, M.; Donner, W.; Durst, K.; Webber, K. G.; Rodel, J. *Journal of the American Ceramic Society* **2016,** 99, (10), 3411-3420.

28. Johnson, K. L., *Contact Mechanics*. Cambridge University Press: Cambridge, London, 1985.

29. W.W.Gerberich; Nelson, J. C.; E.T.Lilleodden; Anderson, P.; J.T.Wyrobek. *Acta Materialia* **1996,** 44, (9), 3585-3598.

30. Kondo, S.; Mitsuma, T.; Shibata, N.; Ikuhara, Y. *Science Advances* **2016**.

31. Wheeler, J. M.; Raghavan, R.; Wehrs, J.; Zhang, Y.; Erni, R.; Michler, J. *Nano letters* **2016,** 16, (1), 812-6.

32. Hertzberg, R. W.; Vinci, R. P.; Hertzberg, J. L., *Deformation and Fracture Mechanics of Engineering Materials*, John Wiley & Sons, Inc., USA, 2013.

33. Schuh, C. A.; Mason, J. K.; Lund, A. C. *Nature Materials* **2005,** 4, (8), 617-21.

34. Njeim, E. K.; Bahr, D. F. *Scripta Materialia* **2010,** 62, (8), 598-601.

35. Wang, C. L.; Lai, Y. H.; Huang, J. C.; Nieh, T. G. *Scripta Materialia* **2010,** 62, (4), 175-178.

36. Prach, O.; Minnert, C.; Johanns, K. E.; Durst, K. *Journal of Materials Research* **2019,** 34, (14), 2492-2500.

37. Rheinheimer, W.; Parras, J. P.; Preusker, J. H.; De Souza, R. A.; Hoffmann, M. J. *Journal of the American Ceramic Society* **2018,** 102, (6), 3779-3790.

38. Rheinheimer, W.; Phuah, X. L.; Wang, H.; Lemke, F.; Hoffmann, M. J.; Wang, H. *Acta Materialia* **2019,** 165, 398-408.

39. Jia, C. L.; Houben, L.; Urban, K. *Philosophical Magazine Letters* **2006,** 86, (11), 683-690.

40. Du, H.; Jia, C. L.; Mayer, J. *Faraday discussions* **2019,** 213, (0), 245-258.

41. Gömann, K.; Borchardt, G.; Gunhold, A.; Maus-Friedrichs, W.; Baumann, H. *Phys. Chem. Chem. Phys.* **2004,** 6, (13), 3639-3644.

42. Gömann, K.; Borchardt, G.; Schulz, M.; Gömann, A.; Maus-Friedrichs, W.; Lesage, B.; Kaitasov, O.; Hoffmann-Eifert, S.; Schneller, T. *Physical chemistry chemical physics : PCCP* **2005,** 7, (9), 2053-60.

43. De Souza, R. A. *Advanced Functional Materials* **2015,** 25, (40), 6326-6342.

44. Cho, J.; Li, J.; Wang, H.; Li, Q.; Fan, Z.; Mukherjee, A. K.; Rheinheimer, W.; Wang, H.; Zhang, X. *Materials Research Letters* **2019,** 7, (5), 194-202.

45. Fang, X.; Kreter, A.; Rasinski, M.; Kirchlechner, C.; Brinckmann, S.; Linsmeier, C.; Dehm, G. *Journal of Materials Research* **2018,** 33, (20), 3530-3536.

46. Scheel, H. J.; Bednorz, J. G.; Dill, P. *Ferroelectrics* **1976,** 13, (1), 507-509.

47. Tanaka, T.; Matsunaga, K.; Ikuhara, Y.; Yamamoto, T. *Physical Review B* **2003,** 68, (20).

48. Moos, R.; Härdtl, K. H. *Journal of the American Ceramic Society* **1997,** 80, (10), 2549-2562.

49. Durst, K.; Maier, V. *Current Opinion in Solid State and Materials Science* **2015,** 19, (6), 340-353.

50. Oliver, W. C.; Pharr, G. M. *Journal of Materials Research* **1992,** 7, (6), 1564-1583.

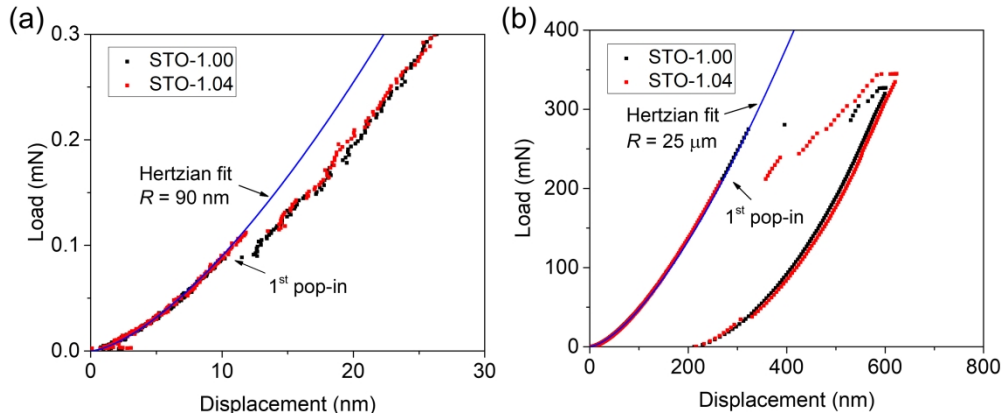

Figure 1

286x119mm (300 x 300 DPI)

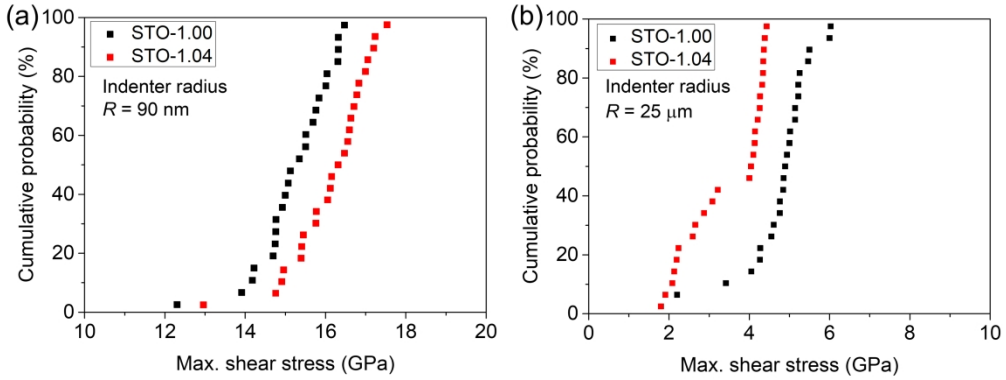

Figure 2

308x119mm (300 x 300 DPI)

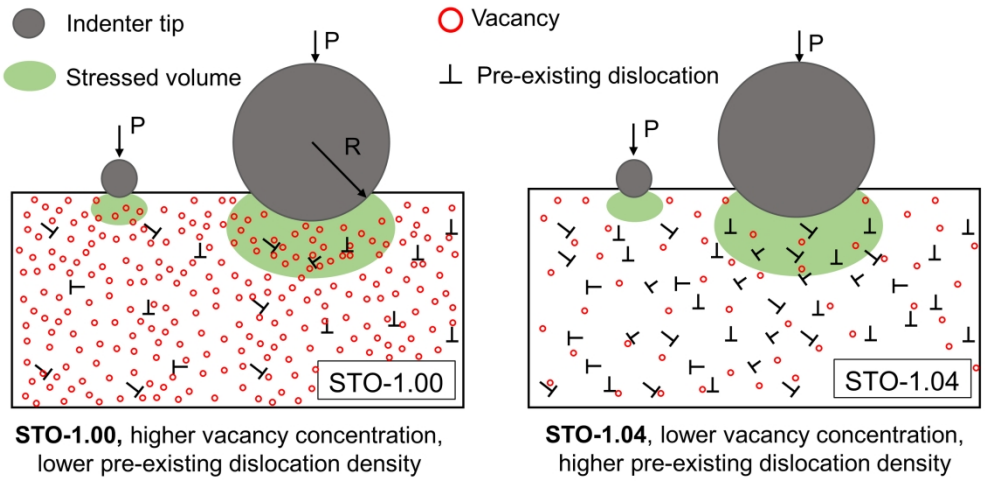

Figure 3

239x114mm (300 x 300 DPI)

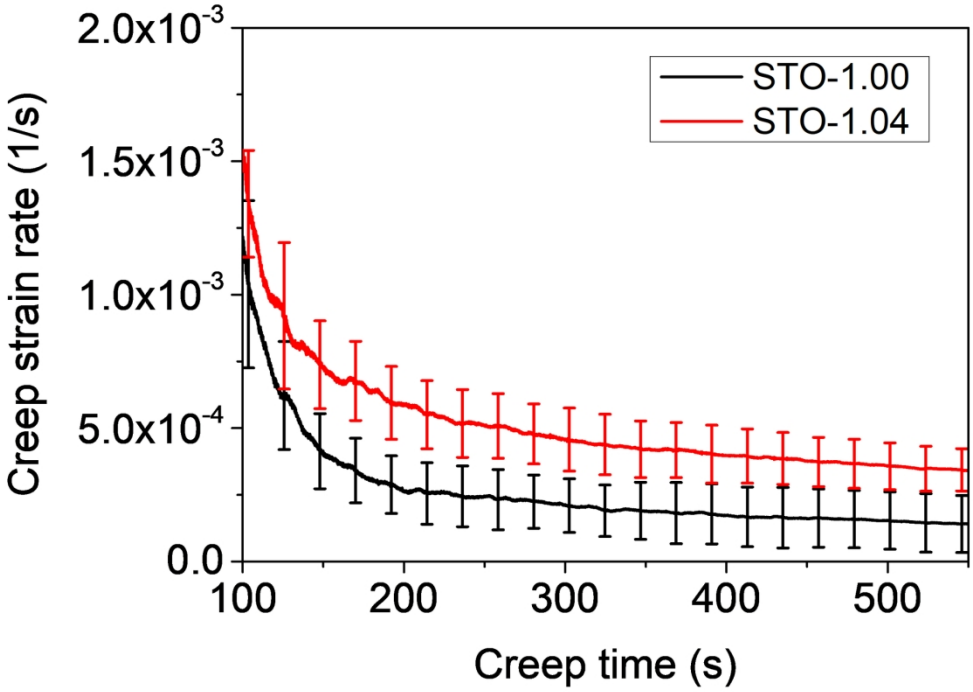

Figure 4

174x123mm (300 x 300 DPI)

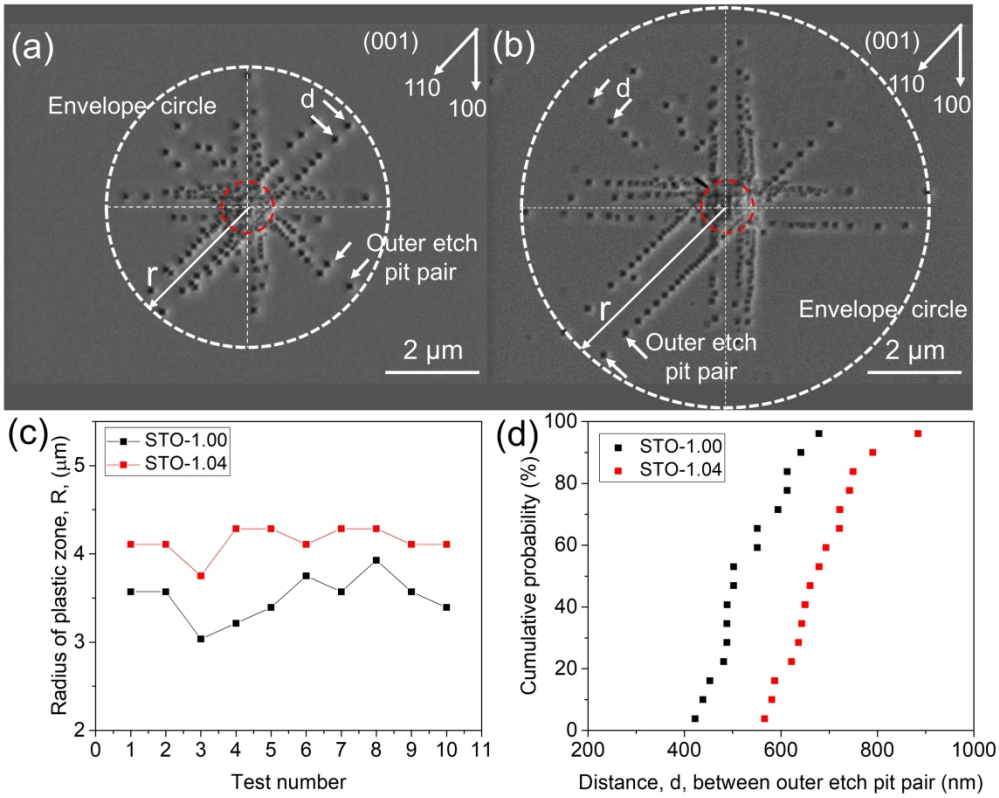

Figure 5

235x187mm (300 x 300 DPI)